JOURNAL OF SPACECRAFT AND ROCKETS
Vol. 36, No. 4, July–August 1999

Detailed Simulation of Surface Chemistry Leading to Spacecraft Glow

Daniel P. Karipides* and Iain D. Boyd†
Cornell University, Ithaca, New York 14853
and
George E. Caledonia‡
Physical Sciences, Inc., Andover, Massachusetts 01810

Glow brightness around the Atmosphere Explorer satellite over the altitude range of 140–300 km is calculated using a multistep approach. The flowfield around the satellite is simulated using the direct simulation Monte-Carlo method. An overlay technique is used to simulate rare atmospheric species with acceptable statistical accuracy. Both nonreactive and reactive surface events are modeled by a system of ordinary differential equations. A simple analytical model is then used to convert a surface flux to glow brightness. A comprehensive set of production mechanisms is included in the calculation of glow brightness for the first time. The effects of satellite rotation are investigated and found to be most significant at higher altitudes. Sensitivity to the surface event parameters is assessed, and the critical production reaction for spacecraft glow is identified. The importance of the freestream concentration of nitric oxide is demonstrated. Very good agreement with experimental data is achieved.

Nomenclature

A^a = species A adsorbed on the surface
A_i = species i, where $1 \leq i \leq N$
$\vec{A}$ = species A moving toward the surface
$\overleftarrow{A}$ = species A moving away the surface
F_i = flux of species i to the surface, particles/(m^{2}s)
K_{ij}^{lh} = Langmuir–Hinshelwood reaction rate for species i and j, m^2/particles
N = number of species
n_i = surface number density of species i
n_s = surface number density of surface sites
Q = species of interest
S_i = sticking coefficient for species i
X = free surface site
ϵ_{ij}^{er} = probability of ejection after Eley–Rideal reaction
ϵ_{ij}^{lh} = probability of ejection after Langmuir–Hinshelwood reaction
Θ_i = surface coverage of species i, identical to n_i/n_s
σ_{ij}^{d} = desorption cross section for species i and j, m^2
σ_{ij}^{er} = Eley–Rideal cross section for species i and j, m^2
τ_i = thermal desorption time for species i, s

Introduction

THE occurrence of an orange–red visible glow around ram surfaces in low Earth orbit has been well documented.[1–3] This spacecraft glow can interfere with optical experiments onboard satellites and could also provide a possible detection mechanism of missiles during reentry. The spectra of spacecraft glow measured on several vehicles are consistent with the spectrum of electronically excited nitrogen dioxide (NO_2^*), red shifted from the gas-phase spectrum.[4] The production of nitrogen dioxide in rarefied, high-speed airflows is a complicated process, involving a number of precursor steps. Detailed modeling of these processes is required to calculate accurately glow brightness in simulated flows. In this study, a three-stage model is used to calculate spacecraft glow. In the first stage, gas–gas collisions in the weak bow shock in front of the ram surface lead to the creation of rare chemical species. In the second stage, these rare species and the species of the bulk gas interact with each other through a complex set of processes that occur on the surface of the spacecraft. The surface events result in a flux of NO_2^* emitted from the surface. In the third stage, this flux is converted into glow brightness using a straightforward model. A Monte Carlo method is used to track the reactions in the weak shock.[5] A Runge–Kutta method is used to solve a set of ordinary differential equations describing the surface events. The solver also incorporates the model that converts the excited nitrogen dioxide flux into a glow brightness.

This paper presents the results of detailed simulations of spacecraft glow, with a focus on the effects of surface chemistry. Details are given of the satellite missions from which experimental data are taken. The surface model is described by giving the types of events that are included and the limiting assumptions employed in the modeling. Numerical and additional modeling considerations are discussed. The results presented include a study of a representative case, sensitivity to model parameters, and comparisons to experimental data.

Atmosphere Explorer Satellite

To provide a source for comparison of the numerical predictions, data are taken from flights of the Atmosphere Explorer (AE) satellites. The AE satellites flew three missions during the 1970s and early 1980s. The satellite body is approximately a cylinder of radius 0.7 m and length 1.0 m. The AE satellites typically flew spin stabilized with the axis of spin perpendicular to the velocity vector. It also flew in a despun mode for particular orbits. Whereas a wide variety of instruments were carried onboard, two experiments are of particular interest here. The first of these is the visible airglow experiment (VAE).[6] Measurements of glow were recorded for several wavelengths. This report focuses on glow measurements at 656.3 and 732.0 nm for the altitude range of 140–300 km. Only the forward-looking glow values are considered here. In this range, the magnitude of the glow varies from $\mathcal{O}(100)$ to $\mathcal{O}(1)$ Rayleighs. A well-known feature of these data is a change in the slope of the glow brightness with altitude at an altitude of about 165 km (Ref. 1). This bend has been attributed to the importance of gas–gas chemical reactions at the lower, more dense altitudes.[5] The second AE experiment of interest is the neutral atmosphere composition experiment (NACE).[7] This experiment measured the ambient concentration of several air species, including nitric oxide. Measurement of nitric oxide concentration is important because its value varies greatly in

Received 29 June 1998; revision received 17 November 1998; accepted for publication 19 November 1998.

*Graduate Student, Department of Mechanical and Aerospace Engineering. Member AIAA.
†Associate Professor, Department of Mechanical and Aerospace Engineering. Member AIAA.
‡President. Associate Fellow AIAA.

the Earth's atmosphere. Therefore, the prediction of the ambient concentration of NO using analytical models is difficult. Indeed, the density values recorded by the NACE show a large scatter at each of the altitudes of interest. This variation provides lower and upper bounds for the NO concentrations, which are used as an input condition for the simulations.

Surface Event Modeling

The glow measurements are consistent with the spectrum of NO_2^*. In flows of rarefied air, NO_2^* is created through reactions involving nitric oxide. Two of the primary candidate surface reactions that lead to the production of nitrogen dioxide are

$$NO + O^a \rightarrow NO_2^* \tag{1}$$

$$O + NO^a \rightarrow NO_2^* \tag{2}$$

where the superscript a indicates the species is adsorbed on the surface. The reaction that dominates depends on the relative concentrations of O and NO, both in the gas phase and on the surface, and on the reaction rates. The gas-phase concentrations are computed using a Monte Carlo method. These concentrations are affected by both the assumed freestream concentrations and the chemical reactions that occur in the flowfield. The surface concentrations are computed using a Runge–Kutta method to solve the system of differential equations described in the next section.

Surface Events

Five types of surface events are considered: physical adsorption, thermal desorption, collisional desorption, gas–surface (Eley–Rideal) reactions, and surface–surface (Langmuir–Hinshelwood) reactions. In this section, each event is classified and described in terms of a general chemical representation. The parameters characterizing the event are then defined. Finally, the effect on the rate of change of surface number density is expressed in differential form.

An adsorption event occurs when a molecule impacting the surface does not reflect, but rather is trapped on the surface. There are several ways in which a molecule may be adsorbed, physical and chemical adsorption being the two primary forms. Any molecule that chemically adsorbs to the surface is tightly bound and much less likely to participate in other surface events. Thus, the only type of adsorption considered in this model is physical adsorption, where the physisorbed species are assumed to form a monolayer on top of the chemisorbed species.[8] A physical adsorption event is represented by

$$\bar{Q} + X \rightarrow Q^a$$

where X symbolizes a free surface site. Each event can be characterized by a sticking coefficient, which is simply the probability that a molecule striking the surface becomes adsorbed. The rate of change of surface number density for species Q is

$$\frac{dn_Q}{dt} = S_Q F_Q \left(1 - \sum_{i=1}^{N} \Theta_i\right) \tag{3}$$

The term in parentheses represents the fraction of adsorption sites that are uncovered and available.

Spontaneous desorption of a physisorbed molecule is termed thermal desorption. Such events occur when the thermal energy of the surface is large enough to overcome the bonding energy of the physisorbed molecule. Symbolically, this is

$$Q^a \rightarrow \bar{Q} + X$$

In this model, thermal desorption events are characterized by a time constant. This characteristic time combines the effect of binding energy and surface temperature. The rate of change of surface number density for species Q is

$$\frac{dn_Q}{dt} = -\frac{n_Q}{\tau_Q} \tag{4}$$

Collisional desorption is desorption that is initiated from the surface through a direct collision with an incident gas-phase molecule. An event of this type can be written

$$\vec{A}_i + Q^a \rightarrow \bar{A}_i + \bar{Q} + X$$

A collision cross section characterizes collisional desorption events. Theoretically, this cross section varies for each type of collision pair. In the present study, this parameter is varied depending only on the adsorbed species. The rate of change of surface number density for species Q due to species i is

$$\frac{dn_Q}{dt} = -F_i n_Q \sigma_{iq}^d \tag{5}$$

Chemical reactions involving an incident gas-phase molecule and an adsorbed molecule are termed Eley–Rideal reactions. The product may stay adsorbed to the surface or may be ejected into the flowfield. Shown symbolically, these are

$$\vec{A}_i + A_j^a \rightarrow \bar{Q} + X$$

$$\vec{A}_i + A_j^a \rightarrow Q^a$$

As with a collisional desorption event, an Eley–Rideal reaction is characterized by a cross section. Each Eley–Rideal reaction results in a reduction of the surface concentration of species A_j. The surface concentration of species Q will increase if the particle remains adsorbed on the surface. Defining ϵ_{ij}^{er} as this probability of ejection into the gas phase of the species Q created from species i and j, the rates of change may be expressed as

$$\frac{dn_Q}{dt} = \left(1 - \epsilon_{ij}^{er}\right) \sigma_{ij}^{er} F_i n_j, \qquad \frac{dn_j}{dt} = -\sigma_{ij}^{er} F_i n_j \tag{6}$$

The final type of surface events considered are Langmuir–Hinshelwood reactions, involving two surface-adsorbed molecules. Similar to gas–surface reactions, the resultant product may stay adsorbed on the surface or may be ejected into the flowfield, or

$$A_i^a + A_j^a \rightarrow \bar{Q} + 2X$$

$$A_i^a + A_j^a \rightarrow Q^a + X$$

Noting that surface–surface reactions are described through a reaction rate as opposed to a cross section, the rates of change become

$$\frac{dn_Q}{dt} = \left(1 - \epsilon_{ij}^{lh}\right) K_{ij}^{lh} n_i n_j, \qquad \frac{dn_i}{dt} = \frac{dn_j}{dt} = -K_{ij}^{lh} n_i n_j \tag{7}$$

It is useful to define a species surface coverage, $\Theta_i \equiv n_i / n_s$, where n_s is the surface number density of available sites. Dividing Eqs. (3–7) by n_s and combining them, the overall rate of change of surface coverage for species Q can be written collectively as

$$\begin{aligned}\frac{d\Theta_Q}{dt} = {} & \frac{S_Q F_Q}{n_s}\left(1 - \sum_{i=1}^{N}\Theta_i\right) - \frac{\Theta_Q}{\tau_Q} - \sum_{i=1}^{N} F_i \Theta_Q \sigma_{iq}^d \\ & + \sum_{i=1}^{N}\sum_{j=1}^{N}\left(1 - \epsilon_{ij}^{er}\right)\sigma_{ij}^{er} F_i \Theta_j - \sum_{i=1}^{N} \sigma_{iQ}^{er} F_i \Theta_Q \\ & + \sum_{i=1}^{N}\sum_{j=i}^{N}\left(1 - \epsilon_{ij}^{lh}\right) n_s K_{ij}^{lh} \Theta_i \Theta_j - \sum_{i=1}^{N} n_s K_{iQ}^{lh} \Theta_i \Theta_Q\end{aligned} \tag{8}$$

Values for the fluxes are determined from the Monte Carlo simulations. A listing of all of the events considered is given in Tables 1 and 2. Baseline values for the parameters in all of the surface events are taken from the report by Gorelev et al.[9] These baseline values represent a collection of values from literature as well as estimates and approximations. To compliment the Gorelev et al. report, values for the parameters of important events are taken from additional sources. In particular, sources were found for nitric oxide adsorption[10–12] and thermal desorption,[13] for molecular oxygen

Table 1 Nonreacting events

Event	Parameter
Physical adsorption	S
$\vec{N}_2 + X \rightarrow N_2^a$ (e1)	0.03
$\vec{O}_2 + X \rightarrow O_2^a$ (e2)	0.03
$\vec{NO} + X \rightarrow \vec{NO}^a$ (e3)	0.3
$\vec{N} + X \rightarrow N^a$ (e4)	0.3
$\vec{O} + X \rightarrow O^a$ (e5)	0.3
Thermal desorption	τ_d, s
$N_2^a \rightarrow \vec{N}_2 + X$ (e6)	0.25
$O_2^a \rightarrow \vec{O}_2 + X$ (e7)	0.25
$\vec{NO}^a \rightarrow \vec{NO} + X$ (e8)	25.00
$N^a \rightarrow \vec{N} + X$ (e9)	25.00
$O^a \rightarrow \vec{O} + X$ (e10)	25.00
$NO_2^a \rightarrow \vec{NO}_2 + X$ (e11)	25.00
Collisional desorption	σ^d, m^2
$\vec{M} + N_2^a \rightarrow \vec{N}_2 + \vec{M} + X$ (e12)	1.0×10^{-19}
$\vec{M} + O_2^a \rightarrow \vec{O}_2 + \vec{M} + X$ (e13)	1.0×10^{-19}
$\vec{M} + \vec{NO}^a \rightarrow \vec{NO} + \vec{M} + X$ (e14)	4.5×10^{-20}
$\vec{M} + N^a \rightarrow \vec{N} + \vec{M} + X$ (e15)	4.5×10^{-20}
$\vec{M} + O^a \rightarrow \vec{O} + \vec{M} + X$ (e16)	4.5×10^{-20}
$\vec{M} + NO_2^a \rightarrow \vec{NO}_2 + \vec{M} + X$ (e17)	4.5×10^{-20}

Table 2 Reacting events

Reactions	Parameter, m^2
Eley–Rideal	σ^{er}
$\vec{N}_2 + O^a + X \rightarrow NO^a + N^a$ (e18)	2.7×10^{-22}
$\vec{O} + N^a \rightarrow NO^a$ (e19)	3.6×10^{-20}
$\vec{N} + O^a \rightarrow NO^a$ (e20)	3.6×10^{-20}
$\vec{O} + NO_2^a \rightarrow NO^a + \vec{O}_2$ (e21)	1.0×10^{-20}
$\vec{N} + O^a \rightarrow \vec{NO}^* + X$ (e22)	2.5×10^{-21}
$\vec{O} + N^a \rightarrow \vec{NO}^* + X$ (e23)	2.5×10^{-21}
$\vec{O} + NO^a \rightarrow NO_2^a$ (e24)	1.0×10^{-21}
$\vec{NO} + O^a \rightarrow NO_2^a$ (e25)	1.0×10^{-21}
$\vec{NO} + O^a \rightarrow \vec{NO}_2^* + X$ (e26)	1.0×10^{-21}
$\vec{NO} + NO^a \rightarrow \vec{NO}_2^* + N^a + X$ (e27)	1.0×10^{-21}
$\vec{O} + NO^a \rightarrow \vec{NO}_2^* + X$ (e28)	1.0×10^{-21}
$\vec{O} + O^a \rightarrow \vec{O}_2 + X$ (e29)	4.5×10^{-20}
Langmuir–Hinshelwood	K^{lh}
$O^a + N^a \rightarrow NO^a + X$ (e30)	5.0×10^{-23}
$N^a + N^a \rightarrow \vec{N}_2 + 2X$ (e31)	5.0×10^{-23}
$O^a + O^a \rightarrow \vec{O}_2 + 2X$ (e32)	5.0×10^{-23}
$O^a + NO^a \rightarrow \vec{NO}_2^* + 2X$ (e33)	5.0×10^{-23}

adsorption[14–19] and thermal desorption,[20] and for molecular nitrogen adsorption.[21] In general, for the cited sources, whose experimental conditions closely match ram-surface satellite conditions, these additional values support the values of the Gorelev et al. report. Therefore, as a baseline case, the Gorelev et al. values are used.

For many of the parameters of the important events, values are not available in the literature. This is especially true for some of the less commonly considered Eley–Rideal reactions and collisional desorption cross sections. In other cases, the studies are for different surface conditions, different temperatures, and include different reaction phenomenon than considered here. In particular, many studies deal with chemisorption and dissociative adsorption, whereas the main adsorption mechanism in this study is physisorption onto an atomic oxygen monolayer. Regardless of these differences, these values are useful for bounding the parameters used. It is important to note that the significance of the surface event modeling described earlier to the present work is that it represents a substantial increase in detail from previous work in Ref. 5.

Simulation Considerations

As outlined in the Introduction, the numerical approach used to implement the model has three distinct stages. The first stage is a Monte Carlo simulation that determines the structure of the flowfield and incident fluxes to the surface. The second stage is an ordinary differential equation solver, employing the Runge–Kutta method. This solver also incorporates the final stage, converting between NO_2^* flux and glow brightness.

Rare Gas-Phase Species

The flowfield around the AE satellite is simulated using the direct simulation Monte Carlo (DSMC) method.[22] The DSMC technique is appropriate for simulating rarefied flows where binary collisions dominate. Many studies have used DSMC to investigate flows exhibiting high degrees of thermal and chemical nonequilibrium.[23,24] The DSMC technique uses a relatively small number of computational particles to represent the molecules of the real gas. Collisions between two computational particles can exchange momentum, exchange internal energy, and lead to chemical reactions. Instantaneous probabilities of collision, exchange, and reaction are chosen to match models from kinetic theory and rates from phenomenological models. Macroscopic properties of the simulated gas are calculated from average values of the particle properties.

The ambient conditions of the Earth's atmosphere in the altitude range of interest are such that some of the species are extremely rare. Here, a rare species is defined as one having density that is at least two orders of magnitude lower than that of the bulk gas. Given the rarefied nature of the flow, the DSMC method is a natural choice for a numerical approach to solve for the flowfield structure. However, there are some fundamental problems with applying the standard DSMC method to a flow with rare species. These problems are overcome by using a DSMC overlay method, which is more fully described in Ref. 5.

Surface Chemistry Including Satellite Rotation

A simple scheme is used to solve the system of ordinary differential equations given by Eq. (8), using a slightly modified version of the fourth-order Runge–Kutta method. One of the key sets of input parameters are the incident fluxes F_i. The base values for these fluxes are determined from the DSMC solutions, providing a strong link between the two stages. Furthermore, the effects of the satellite rotation must be accounted for if flights of the AE satellite are to be simulated accurately. Thus, these base fluxes are modified by a piecewise function consisting of a sinusoidal term for the forward-half of the rotation and a null term for the back-half of the rotation. The rotation has the overall effect of reducing the total flux to the surface in comparison to the despun case.

Conversion from Surface Flux to Glow Brightness

To make a direct comparison with the VAE data, the emitted flux of NO_2^* must be converted into a glow brightness. The measured glow brightness is given in units of Rayleighs, defined as

$$1 \text{ Rayleigh} \equiv \frac{10^6 \text{ photons}}{\text{cm}^2 \cdot \text{s}}$$

Dimensional considerations suggest a form for the conversion model. First, the simplifying assumption is made that each NO_2^* molecule decays to the ground state and emits a photon within a very short timescale. Thus, a direct conversion from molecules to photons can be made. Second, the probability that an emitted photon has a wavelength within a particular range is given by the ratio of line width area to the total NO_2^* spectrum area (see Fig. 1). The spectrum used is that of a red-shifted NO_2^* spectrum, as described in Ref. 25. In the present study, the glow at 656.3 and 732.0 nm is considered. The photometer in the VAE experiment has a line width of 2 nm. For these wavelengths, the area ratios are approximately $\frac{1}{130}$ and $\frac{1}{100}$, respectively. Thus the final conversion is

$$\text{flux}\left[\frac{\text{particles}}{\text{m}^2 \cdot \text{s}}\right] \times \begin{pmatrix}\text{area}\\ \text{ratio}\end{pmatrix} \times \left(\frac{1}{10^{10}}\right) = \text{flux[Rayleighs]} \quad (9)$$

Results

Multiple simulations of the flowfield around the AE satellite are performed over the altitude range of 140–300 km, with more focus. Two sets of ambient conditions are considered at each altitude, corresponding to a low and a high nitric oxide concentration in the freestream. These ambient concentrations for NO are determined using data from the NACE experiment conducted onboard the AE satellite. Values are listed in Table 3 for reference. All other concentrations are determined using the Mass Spectrometer and Incoherent Scatter (MSIS) model.[26]

Table 3 Ambient NO concentrations measured by NACE

Altitude, km	Low density, $m^{-3} \times 10^{-12}$	High density, $m^{-3} \times 10^{-12}$
140	8	30
150	5	25
160	3	25
170	3	20
180	2	20
190	2	20
200	1	15
250	1	12.5
300	0.7	10

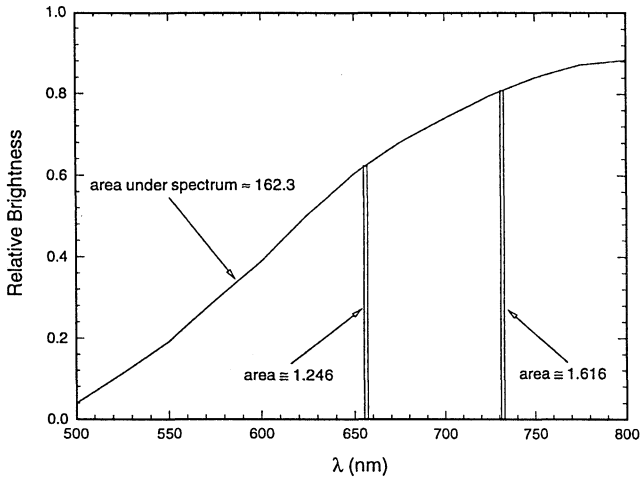

Fig. 1 NO_2^* spectrum and photometer line widths.

The results from these simulations are examined in three sections. First, a representative case is chosen and studied in detail, with particular emphasis being given to the effects of satellite rotation. Second, the sensitivity of the predicted glow brightness to the event parameters is assessed. Finally, a comparison is made between the simulated glow brightness and experimental measurements taken during flights of the AE satellite.

Detailed Study of a Representative Case

The 140-km, high-NO-concentration case is chosen for the representative case. Because this case has the highest ambient density of all of the cases considered, chemical effects should be the most visible. For purposes of contrast, the 140-km, high-NO-concentration case is compared with the 300-km, low-NO case. In both cases, the initial surface coverage of all species is zero. Although the assumption of a clean surface is certainly not to be expected for the real satellite surface, it does provide a uniform starting condition.

Figure 2 shows time-accurate results for glow brightness. Both despun and rotational predictions are shown for each altitude. Comparing the despun results for both 140 and 300 km shows the brightness reaches its steady-state value very quickly at 140 km; at 300 km relatively more time is required. This difference in time is a direct consequence of the higher incident flux at 140 km. The 140-km rotational results exhibit the expected qualitative behavior, showing a cyclic variation with a period of 15 s. Two distinct phenomena are evident. For each half-period, corresponding to when the detector is exposed to the incoming flux, the brightness rises to a maximum value and then decreases. Note that the peak value occurs slightly after the time of maximum flux, due to the inherent timescale of the chemical processes leading from incident fluxes to glow production. The other half-period shows a log-linear decrease in glow, corresponding to when the detector is in the shadow of the satellite and thermal desorption dominates. In the first half-period, the glow at 140 km is greater than the glow at 300 km, as expected. In the second half-period, this is not the case. This initially counterintuitive result is understood through an examination of the relative fluxes of the different species at the two altitudes. At 300 km, the flux of NO and O relative to the total flux is greater

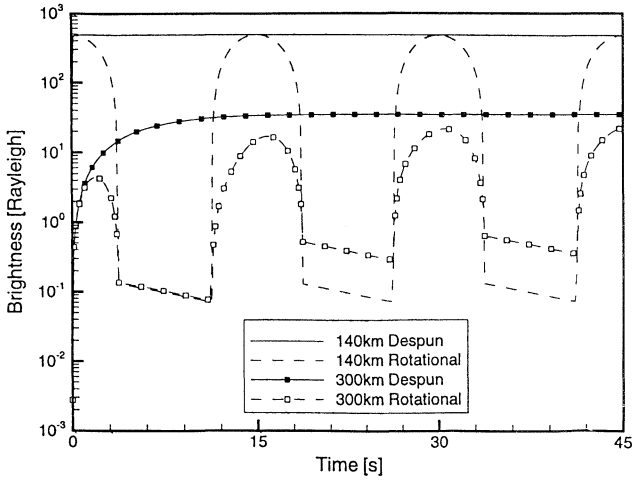

Fig. 2 Effects of satellite rotation on glow brightness.

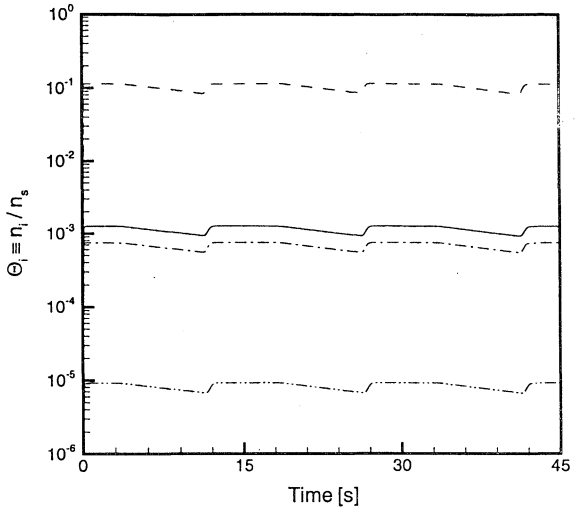

Fig. 3 Effects of satellite rotation on fractional surface concentrations of NO, N, O, and NO_2: ——, Θ(NO); – · –, Θ(N); – – –, Θ(O); and – · · –, Θ(NO_2).

than it is at 140 km. This leads to a higher surface concentration of these species, which results in a higher glow brightness due to event (e33). A more complete analysis of this behavior is available in Ref. 27. As a final comparison, the peak glow values in the rotational case at 140 km match the despun steady-state value. This is not the case at 300 km. Again, this is attributed to the lower flux at 300 km.

Surface coverages for all six species at 140 km are shown in Figs. 3 and 4. Atomic oxygen is the dominant species, with a coverage one order of magnitude greater than N_2 at peak value and at least two orders of magnitude greater than all other species. However, even with the high incident flux at 140 km, the surface coverage of atomic oxygen is only approximately 10%, indicating that the surface is primarily uncovered at all altitudes. Also notable is the disparate behavior of N_2 and O_2 from the other species. Both of these species have relatively low thermal desorption times. Thus, when the surface is rotated away from the incident flux, their coverages drop rapidly, giving the cyclic variability shown in Fig. 4.

A direct comparison of the time-accurate surface coverages at different altitudes is not particularly informative. The disparate behavior of N_2 and O_2 from the other species is seen at all altitudes. It is more illustrative to compare relative steady-state surface concentrations of the species with altitude. Figure 5 shows this comparison. For clarity, molecular nitrogen and oxygen are shown with symbols. The relative surface concentration of these two species decreases with altitude, which follows directly from the lower ambient concentrations at the higher altitudes. Similarly, the increase in the surface coverages for atomic nitrogen and oxygen can be explained

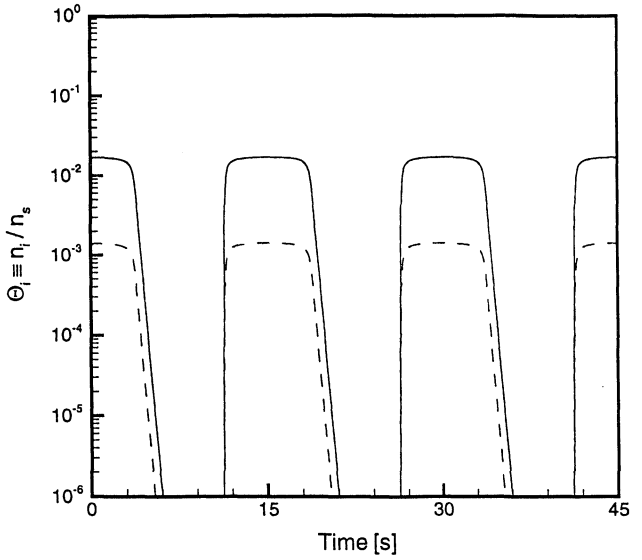

Fig. 4 Effects of satellite rotation on fractional surface concentrations of N_2 and O_2: ——, $\Theta(N_2)$; and – – –, $\Theta(O_2)$.

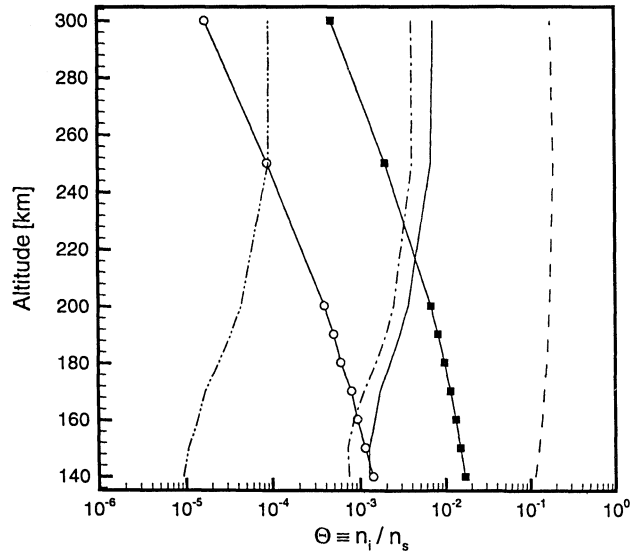

Fig. 5 Variation of surface concentrations with altitude: ■, $\Theta(N_2)$; ○, $\Theta(O_2)$; ——, $\Theta(NO)$; – · –, $\Theta(N)$; – – –, $\Theta(O)$; and – · · –, $\Theta(NO_2)$.

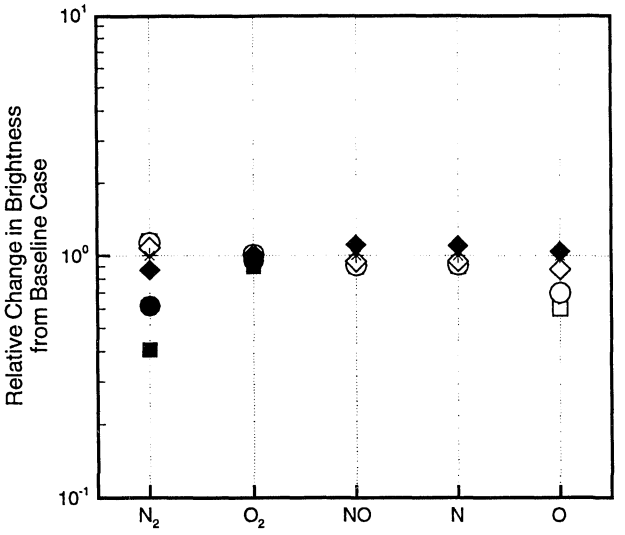

Fig. 6 Sensitivity of brightness to sticking coefficients. Change to sticking coefficient: □, ×0.1; ○, ×0.2; ◇, ×0.5; ∗, ×1.0; ◆, ×2.0; ●, ×5.0; and ■, ×10.0.

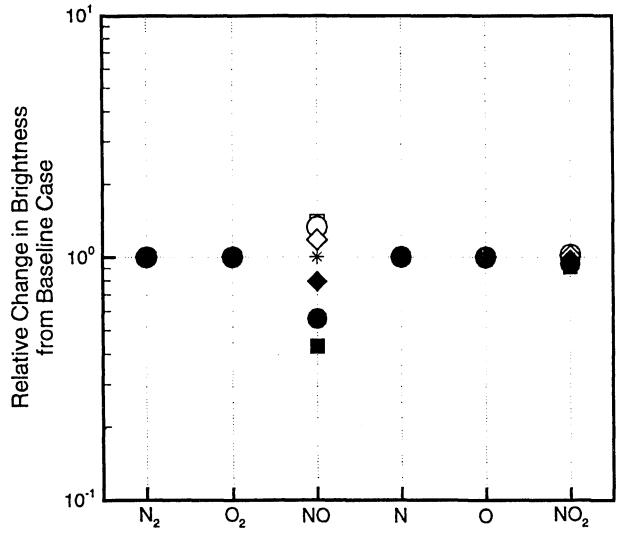

Fig. 7 Sensitivity of brightness to inverse thermal desorption times. Change to inverse thermal desorption time: □, ×0.1; ○, ×0.2; ◇, ×0.5; ∗, ×1.0; ◆, ×2.0; ●, ×5.0; and ■, ×10.0.

from the higher atmospheric concentrations of these species at the higher altitudes. The increased coverages of N and O lead to the increased surface concentration of NO via the Eley–Rideal reactions (e19) and (e20). This, in turn, results in an increase in the concentration of NO_2 due to reactions (e24) and (e25).

As a final look into the representative case at 140 km, the orbital speed of the satellite in the DSMC simulation was lowered from 8 to 7.2 km/s. This lower value may be more reasonable considering the corotation of the atmosphere.[28] Given this reduction of orbital velocity by 10%, the glow production behaves as expected, with reduction in peak glow brightness of approximately 11%. The small difference is due to reduced gas–gas chemistry. This close correspondence also indicates that additional simulations with varied orbital speeds are unnecessary at any altitude.

Sensitivity to Event Parameters

Given the large number of surface events, shown in Tables 1 and 2, it is useful to study the sensitivity of the glow brightness to the event parameters. From this sensitivity study, the important events are identified. For each event, the corresponding parameter is multiplied by the factors 0.1, 0.2, 0.5, 2, 5, and 10. Incidences where this multiplicative factor leads to unphysical values of the parameter are ignored. A complete surface event simulation is performed for each modified value. The 140-km, low-NO-concentration DSMC simulation is used to determine the incident fluxes. Sensitivity is assumed to be similar at other altitudes.

An examination of all of the surface events shows that events (e26), (e27), (e28), and (e33) are the reactions that lead directly to the production of NO_2^*. These reactions are referred to as the production reactions. The only reactants in all of these reactions are NO and O. It is expected that the glow brightness will be most sensitive to parameters of events relating to these two species.

The sensitivity to the sticking coefficients of the freestream species is shown in Fig. 6. Glow brightness is most sensitive to two of the coefficients, those for N_2 and O. For atomic oxygen, the brightness is proportional to the sticking coefficient. Increased atomic oxygen surface coverage enhances production reactions (e26) and (e33). For molecular nitrogen, the brightness is inversely proportional to the sticking coefficient. Molecular nitrogen acts as an inhibitor because it is not a direct precursor to glow and adsorbed N_2 competes with precursors for free surface sites. It is an important inhibitor simply because it is the second most common species in the altitude range of interest.

Figure 7 shows the sensitivity to the inverses of the thermal desorption times. The brightness is seen to be only sensitive to the thermal desorption time for NO. Accounting for the variation shown being for the inverse desorption times, it is evident that increasing the time leads to an increase in glow production. Adsorbed NO is a

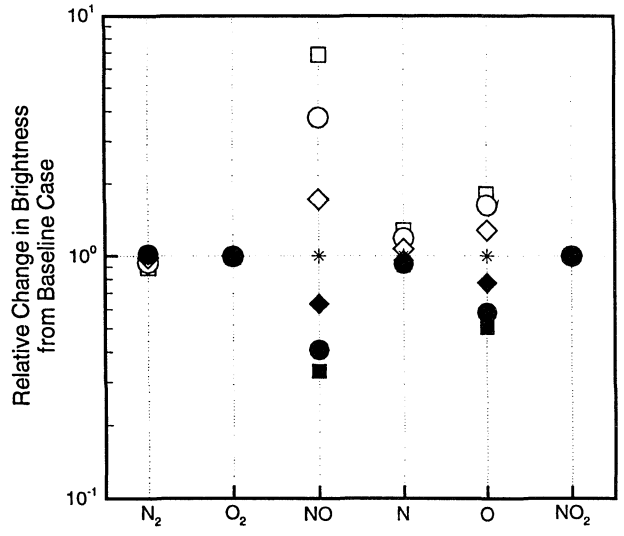

Fig. 8 Sensitivity of brightness to collisional desorption cross sections. Change to collisional desorption cross section: □, ×0.1; ○, ×0.2; ◇, ×0.5; ∗, ×1.0; ◆, ×2.0; ●, ×5.0; and ■, ×10.0.

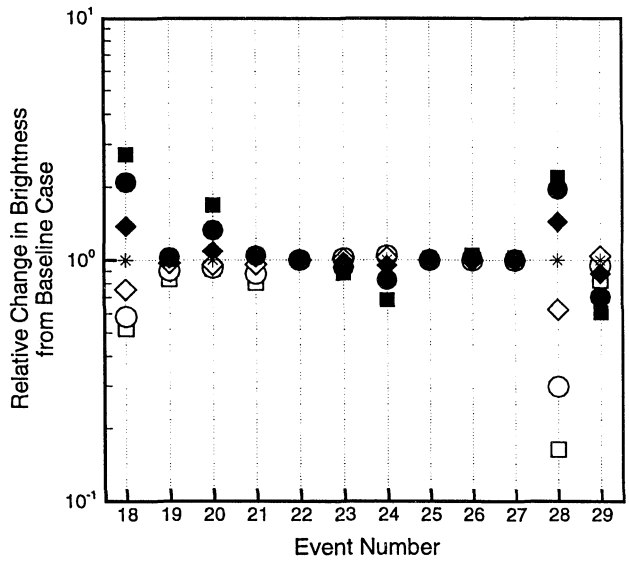

Fig. 9 Sensitivity of brightness to Eley–Rideal cross sections. Change to Eley–Rideal reaction rate: □, ×0.1; ○, ×0.2; ◇, ×0.5; ∗, ×1.0; ◆, ×2.0; ●, ×5.0; and ■, ×10.0.

reactant in production reactions (e27), (e28), and (e33), and so an increased lifetime on the surface leads to greater production of glow.

The effect of varying the collisional desorption cross sections is given in Fig. 8. For these events, the glow production is sensitive to cross sections for both NO and O and in particular NO. Both species show that the glow is inversely proportional to the cross sections. Given that NO and O are the only reactants of the production reactions, this sensitivity result is not surprising.

Figure 9 shows the sensitivity to the cross sections for all of the Eley–Rideal reactions, events (e18–e29). The glow brightness increases with an increase in the cross sections for events (e18), (e20), and (e28). The first two of these reactions lead to an increase in the surface coverage of nitric oxide. The last of these reactions is a production reaction and leads directly to the formation of NO_2^*. The magnitude of the sensitivity to this event identifies it as the primary production reaction. The importance of this reaction is consistent with the findings in Ref. 29. The glow production is reduced with an increase in the cross section of reaction (e24). This reaction reduces the surface coverage of nitric oxide.

The calculated glow brightness shows little sensitivity to the Langmuir–Hinshelwood reaction rates. This behavior is to be expected after an examination of the governing system of ordinary differential equations (8). The term corresponding to production from a surface–surface reaction contains the expression

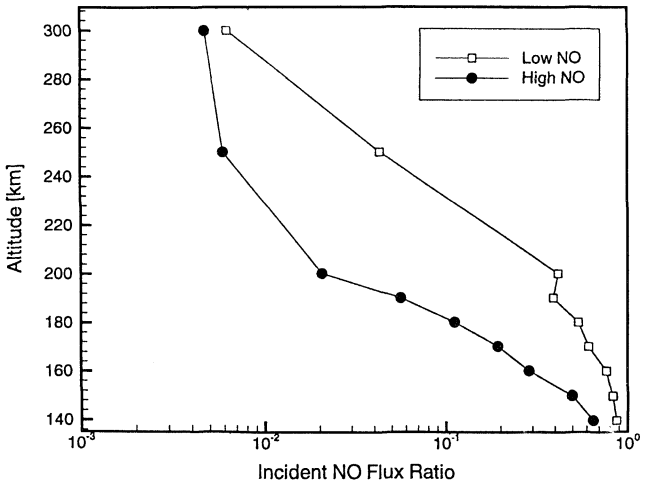

Fig. 10 Contribution of chemically produced NO to total incident NO flux.

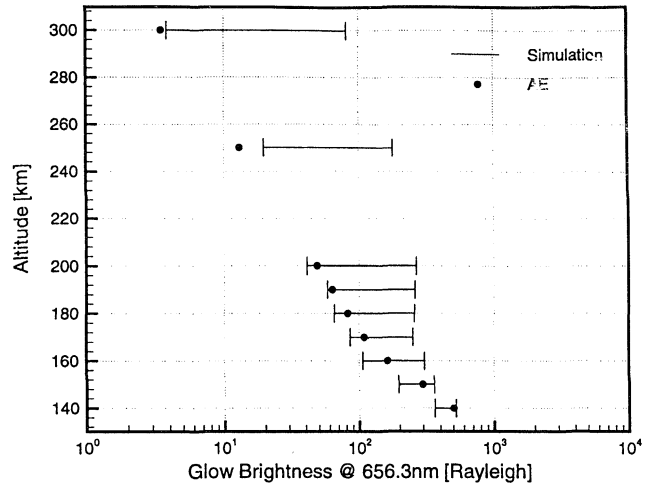

Fig. 11 Comparison of predicted glow brightness to AE data at 656.3 nm.

$(1-\epsilon_{ij}^{lh})n_s K_{ij}^{lh}\Theta_i\Theta_j$. Because n_s is $\mathcal{O}(10^{19})$, K is $\mathcal{O}(10^{-23})$, and all other terms are $\mathcal{O}(1)$, the magnitude of this term will be of $\mathcal{O}(10^{-4})$. A similar analysis of another term, e.g., the expression for collisional desorption, gives a magnitude as high as $\mathcal{O}(10^{-1})$. Thus, it is not surprising that Langmuir–Hinshelwood reactions have a limited effect on the overall glow production.

Comparison to AE Data

The incident flux of nitric oxide that participates in the production of glow has two sources. Nitric oxide is found in limited concentrations in the ambient atmosphere. As was mentioned earlier, these concentrations vary significantly due to solar activity, magnetic cycles, and other phenomena. Again, for this reason, the ambient concentrations of NO are taken from the NACE experiment. Nitric oxide is also produced chemically in the weak shock in front of the vehicle. At the higher altitudes, the flow is almost collisionless, and the production of NO in the weak shock is negligible. Thus, almost all of the NO in the flowfield is ambient NO. At the lower altitudes, a significant portion of the NO in the flowfield is produced through gas–gas reactions. This behavior is quantified in Fig. 10. The plot shows the fraction of the total incident NO flux that is chemically produced NO. Values for both the low and high ambient nitric oxide concentrations are plotted. As expected, this fraction decreases as altitude decreases.

The steady-state values for glow brightness at 656.3 nm using both ambient NO concentrations are compared to experimental data from the AE satellite in Fig. 11. The calculated values agree well with the measured glow brightness, representing a substantial improvement over the previous results presented in Ref. 5. This improvement is a direct consequence of the more detailed modeling. Furthermore,

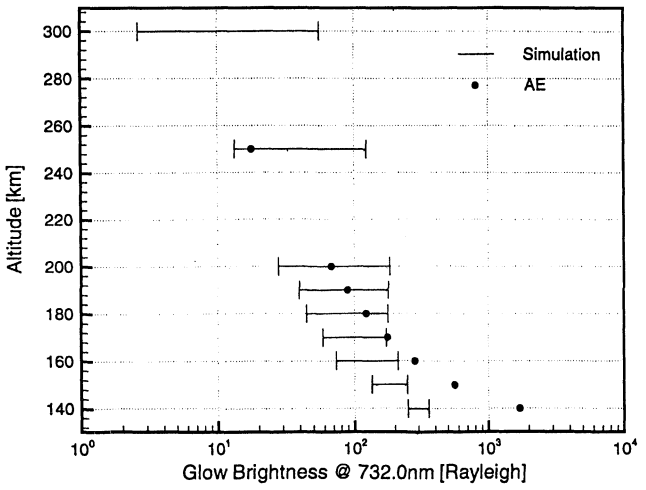

Fig. 12 Comparison of predicted glow brightness to AE data at 732.0 nm.

the sensitivity to the ambient concentration of NO is greater at the higher altitudes. This sensitivity is a direct result of the chemically produced NO being less significant at the higher altitudes, magnifying the importance of fluctuations in the ambient concentrations.

Figure 12 compares the simulated values for glow brightness to the experimental measurements at the 732.0-nm wavelength. At this wavelength, the calculated values also agree well with measurements at altitudes above 160 km. At the lower altitudes, there is an underprediction. This indicates that the surface reactions and events responsible for the production of glow are too infrequent at the lower altitudes. The sensitivity of the brightness at the higher altitudes to the ambient NO concentration is also seen at this wavelength.

Conclusions

This study represents the first detailed computation of spacecraft glow that includes a comprehensive set of production mechanisms. From the examination of the representative case, the chosen simulation method was shown to be qualitatively valid. The effects of satellite rotation were effectively captured. In terms of the forward-looking glow brightness, these effects were more important at the higher altitudes. The behavior of the species surface concentrations were found to strongly depend on the magnitude of the thermal desorption time constants. Relative concentrations varied with altitude according to ambient densities and specific surface events.

The sensitivity study showed that parameters relating to nitric oxide and atomic oxygen are the most important values in determining the glow brightness. Again, this is as expected, because NO and O are the only reactants in the production reactions. Specifically, the events (e1), (e5), (e8), (e14), (e16), (e18), and (e20) were identified as the critical precursor events. Furthermore, the Eley–Rideal reaction $\vec{O} + NO^a \rightarrow \hat{NO}_2^* + X$ (e28) was found to be the dominant production reaction. The insignificance of the Langmuir–Hinshelwood reactions was explained through an order of magnitude analysis of the governing differential equations.

The importance of the ambient concentration of nitric oxide at the higher altitudes was clear. Comparison of the predicted brightness values to data taken by the VAE onboard the AE satellite was very good. The agreement of the calculated glow brightness to experimental measurements represented a significant improvement over previous numerical predictions.

Acknowledgments

Funding for this work was provided by the Ballistic Missile Defense Organization under Augmentation Awards for Science and Engineering Research Training Award DAAH04-95-1-0204. Computational resources were provided on an IBM SP-2 at the Cornell Theory Center.

References

[1]Yee, J. H., and Abreu, V. J., "Visible Glow Induced by Spacecraft–Environment Interaction," *Geophysical Research Letters*, Vol. 10, No. 2, 1983, pp. 126–129.

[2]Yee, J. H., Abreu, V. J., and Dalgarno, A., "Characteristics of the Spacecraft Optical Glow," *Geophysical Research Letters*, Vol. 11, No. 12, 1984, pp. 1192–1194.

[3]Garret, H. B., Chutjian, A., and Gabriel, S., "Space Vehicle Glow and Its Impact on Spacecraft Systems," *Journal of Spacecraft and Rockets*, Vol. 25, No. 5, 1988, pp. 321–340.

[4]Caledonia, G. E., Holtzclaw, K. W., Krech, R. H., and Sonnenfroh, D. M., "Mechanistic Investigations of Shuttle Glow," *Journal of Geophysical Research*, Vol. 98, No. A3, 1993, pp. 3725–3730.

[5]Karipides, D. P., Boyd, I. D., and Caledonia, G. E., "Development of a Monte Carlo Overlay Method with Application of Spacecraft Glow," *Journal of Thermophysics and Heat Transfer*, Vol. 12, No. 1, 1998, pp. 30–37.

[6]Hays, P. B., Carignan, G., and Kennedy, B. C., "The Visible-Airglow Experiment on Atmosphere Explorer," *Radio Science*, Vol. 8, No. 4, 1973, pp. 369–377.

[7]Pelz, D. T., Reber, C. A., and Hedin, A. E., "A Neutral-Atmosphere Composition Experiment for the Atmosphere Explorer-C, -D and -E," *Radio Science*, Vol. 8, No. 4, 1973, pp. 277–285.

[8]Dogra, V. K., Collins, R. J., and Levin, D. A., "Simulations of Spacecraft Rarefied Environments Using a Proposed Surface Model," AIAA Paper 98-0834, Jan. 1998.

[9]Gorelev, K., Karabadzhak, G., Kireev, A., Nikolsky, V., Plastin, Y., and Yegorov, I., "Modeling of NO, N_2, NO_2 Molecules Band Emission in Shock Layers," Central Research Inst. of Engineering Industry, TSNI-IMASH CR A935-21, Kaliningrad, Russia, 1995.

[10]Sharpe, R. G., and Bowker, M., "The Adsorption and Decomposition of NO on Pd(110)," *Surface Science*, Vol. 360, No. 1–3, 1996, pp. 21–30.

[11]Bowker, M., Guo, Q., and Joyner, R. W., "NO Adsorption on Rh(110)," *Surface Science*, Vol. 257, No. 1–3, 1991, pp. 33–40.

[12]Wartnaby, C. E., Stuck, A., Yeo, Y. Y., and King, D. A., "Microcalorimetric Heats of Adsorption for CO, NO and Oxygen on Pt110," *Journal of Physical Chemistry*, Vol. 100, No. 30, 1996, pp. 12,483–12,488

[13]Luo, M., Zhong, Y., Zhu, B., Yuan, X., and Zheng, X., "Temperature-Programmed Desorption Study of NO and CO2 over CeO2 and ZrO2," *Applied Surface Science*, Vol. 115, No. 2, 1997, pp. 185–189.

[14]Artsyukhovich, A. N., Ukraintsev, V. A., and Harrison, I., "Low Temperature Sticking and Desorption Dynamics of Oxygen on Pt(111)," *Surface Science*, Vol. 347, No. 3, 1996, pp. 303–318.

[15]Buatier de Mongeot, F., Rocca, M., Cupolillo, A., Valbusa, U., Kreuzer, H. J., and Payne, S. H., "Sticking and Thermal Desorption of O_2 on Ag(001)," *Journal of Chemical Physics*, Vol. 106, No. 2, 1997, pp. 711–718.

[16]Butler, D. A., Sanders, J. B., Raukema, A., Kleyn, A. W., and Frenken, J. W. M., "Oxygen Dissociation on Ag(110): a Ruin Game," *Surface Science*, Vol. 375, No. 2–3, 1997, pp. 141–149.

[17]Pazzi, V. I., and Tantardini, G. F., "Dynamical Simulations of the Oxygen Adsorption on the Ag(110) Surface," *Journal of Molecular Catalysis, A: Chemical*, Vol. 119, No. 1–3, 1996, pp. 289–297.

[18]Pazzi, V. I., and Tantardini, G. F., "Dynamics of Oxygen Adsorption on Ag(110): Surface Motion Effects," *Surface Science*, Vol. 377–379, No. 1–3, 1996, pp. 572–577.

[19]Sjovall, P., and Uvdal, P., "Oxygen Sticking on Pd(111): Double Precursors, Corrigation and Substrate Temperature Effects," *Chemical Physics Letters*, Vol. 282, No. 5–6, 1998, pp. 355–360.

[20]He, J.-W., and Norton, P. R., "Thermal Desorption of Oxygen from a Pd(110) Surface," *Surface Science*, Vol. 204, No. 1–2, 1988, pp. 26–34.

[21]Dietrich, H., Geng, P., Jacobi, K., and Ertl, G., "Sticking Coefficient for Dissociative Adsorption of N2 on Ru Single-Crystal Surfaces," *Journal of Chemical Physics*, Vol. 104, No. 1, 1996, pp. 375–381.

[22]Bird, G. A., *Molecular Gas Dynamics and the Direct Simulation of Gas Flows*, Oxford Univ. Press, New York, 1994, pp. 203–407.

[23]Boyd, I. D., "Analysis of Rotational Nonequilibrium in Standing Shock Waves of Nitrogen," *AIAA Journal*, Vol. 28, No. 11, 1990, pp. 1997, 1998.

[24]Boyd, I. D., Candler, G. V., and Levin, D. A., "Dissociation Modeling in Low Density Flows of Air," *Physics of Fluids*, Vol. 7, No. 7, 1995, pp. 1757–1763.

[25]Kenner, R. D., and Orgylzo, E. A., "Orange Chemiluminescence from NO_2," *Journal of Chemical Physics*, Vol. 80, No. 1, 1984, pp. 1–6.

[26]Hedin, A. E., "The Atmospheric Model in the Region 90 to 2000km," *Advances in Space Research*, Vol. 8, Nos. 5–6, 1988, pp. 9–25.

[27]Karipides, D. P., "Detailed Simulation of Spacecraft Glow," Ph.D. Dissertation, Sibley School of Mechanical and Aerospace Engineering, Cornell Univ., Ithaca, NY, May 1999.

[28]Murad, E., "Spacecraft Interaction with Atmospheric Species in Low Earth Orbit," *Journal of Spacecraft and Rockets*, Vol. 33, No. 1, 1996, pp. 131–136.

[29]Murad, E., "The Shuttle Glow Phenomenon," *Annual Review of Physical Chemistry*, Vol. 49, 1998, pp. 73–98.

R. G. Wilmoth
Associate Editor